

# Kinesthetic Feedback during 2DOF Wrist Movements via a Novel MR-Compatible Robot

Andrew Erwin, *Student Member, IEEE*, Marcia K. O'Malley, *Senior Member, IEEE*, David Ress, *Senior Member, IEEE*, and Fabrizio Sergi, *Member, IEEE*

**Abstract**—We demonstrate the interaction control capabilities of the MR-SoftWrist, a novel MR-compatible robot capable of applying accurate kinesthetic feedback to wrist pointing movements executed during fMRI. The MR-SoftWrist, based on a novel design that combines parallel piezoelectric actuation with compliant force feedback, is capable of delivering 1.5 N·m of torque to the wrist of an interacting subject about the flexion/extension and radial/ulnar deviation axes. The robot workspace, defined by admissible wrist rotation angles, fully includes a circle with a 20 deg radius. Via dynamic characterization, we demonstrate capability for transparent operation with low (10% of maximum torque output) backdrivability torques at nominal speeds. Moreover, we demonstrate a 5.5 Hz stiffness control bandwidth for a 14 dB range of virtual stiffness values, corresponding to 25-125% of the device's physical reflected stiffness in the nominal configuration. We finally validate the possibility of operation during fMRI via a case study involving one healthy subject. Our validation experiment demonstrates the capability of the device to apply kinesthetic feedback to elicit distinguishable kinetic and neural responses without significant degradation of image quality or task-induced head movements. With this study, we demonstrate the feasibility of MR-compatible devices like the MR-SoftWrist to be used in support of motor control experiments investigating wrist pointing under robot-applied force fields. Such future studies may elucidate fundamental neural mechanisms enabling robot-assisted motor skill learning, which is crucial for robot-aided neurorehabilitation.

**Index Terms**—MR-compatible robotics, compliant actuators, force control, haptics, functional MRI (fMRI).

## I. INTRODUCTION

**S**INCE the advent of functional magnetic resonance imaging (fMRI) in the early 1990s, neuroscientists have been able to non-invasively study neural activity of the entire brain with high spatial resolution [1], starting with tasks such as recognition and memory [2]. Shortly after, fMRI was also applied to the study of neural activity during human motor control. In one such study, researchers examined the difference in neural activity during rhythmic and discrete movements through one degree of freedom (DOF) wrist flexion/extension (FE) movements [3], while another study used finger tapping or wrist flexion to examine differences in brain activity of patients with chronic stroke pre- and post-therapy [4]. More recently, researchers performed the first multi-DOF visually

This work was supported in part by a TIRR Memorial Hermann Pilot Grant, by the NSF GRFP under Grant No. 1450681, and by the NSF CNS-1135916.

A. Erwin and M. K. O'Malley are with the Mechatronics and Haptic Interfaces Laboratory, Department of Mechanical Engineering, Rice University, Houston, TX 77005 USA (email: ace7@rice.edu; omalley@rice.edu).

D. Ress is with the Department of Neuroscience, Baylor College of Medicine, Houston, TX, 77030 USA (email: ressb@bcm.edu).

F. Sergi is with the Human Robotics Laboratory, Department of Biomedical Engineering, University of Delaware, Newark, Delaware 19713 USA (email: fabs@udel.edu).

## LIST OF ACRONYMS

ADL	Activities of Daily Living	PM	Premotor Cortex
BA	Brodman Area	RF	Radio Frequency
DOF	Degrees of Freedom	RUD	Radial/Ulnar Deviation
EA	Error Augmentation	SEA	Series Elastic Actuator
FE	Flexion/Extension	SS	Somatosensory
FK	Forward Kinematics	TE	Echo Time
fMRI	functional Magnetic Resonance Imaging	TR	Repetition Time
JS	Joint Space	USM	Ultrasonic Motor
MPRAGE	Magnetization-Prepared Rapid Acquisition with Gradient Echo	VC	Visual Control
PC	Path Control	ZF	Zero Force

guided task with the wrist during fMRI to study motor acuity during a semicircular arc pointing task [5]. Among the potential applications for fMRI in the study of motor control, using fMRI to study neuroplastic changes induced by motor neurorehabilitation may be one of the fields to benefit the most. To date, studies examining cortical reorganization over the course of therapy have only been able to use passive devices to measure fMRI pre- and post-therapy [6], [7].

While previous fMRI motor control studies yielded results that expanded our understanding of the neural correlates of motor skill learning, they still lacked a critical component – the controlled combination of kinematic measurement and kinesthetic feedback. Since it is known that variation in amplitude and velocity of movements can modulate brain activation patterns [8], it is important to have knowledge of limb kinematics to account for confounding factors when analyzing brain activity. Additionally, kinesthetic feedback is vital for exploring the world around us, and is especially important in robot-aided neurorehabilitation, a promising approach to motor rehabilitation [9]. Investigation of sensorimotor learning under kinesthetic feedback via fMRI requires an MR-compatible haptic device to apply force fields, while accurately measuring movement kinematics. Researchers have already demonstrated viability in using haptic robots to study motor control outside of an MRI scanner [10], paving the way for the field of haptic fMRI, which studies neural activity during physical human-robot interactions.

Combining haptic robots with fMRI requires special considerations. The principle of fMRI is based on measuring the blood oxygen level dependent signal [2], which is accomplished by measuring inhomogeneities of the MR machine's large static magnetic field (up to 9.4 T for human studies), and requires switching magnetic field gradients and radio frequency (RF) pulses. Any robot used during fMRI must be MR-safe (i.e. it does not pose any threat to the subject) and

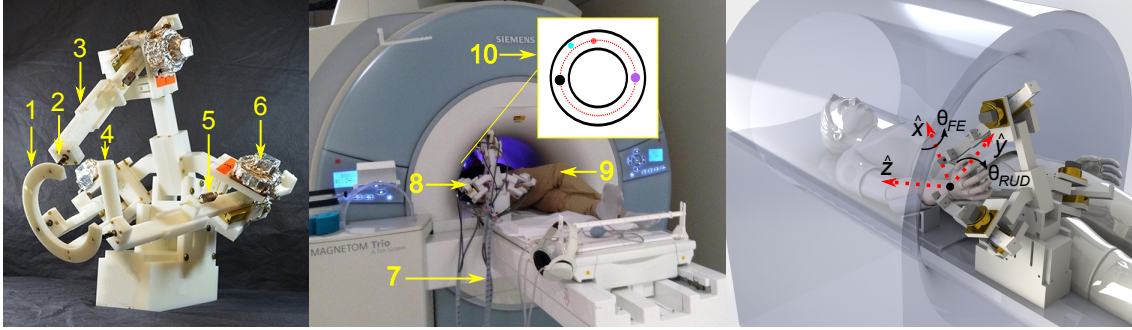


Fig. 1. (left) MR-SoftWrist. 1) Wrist ring, 2) universal joint, 3) link, 4) handle, 5) extension spring, and 6) ultrasonic motor. (center) Subject interacting with the MR-SoftWrist during an fMRI experiment. 7) Encoder and power lines, 8) MR-SoftWrist, 9) subject, and 10) visual display displaying the user's desired and real positions. (right) CAD rendering of a subject interacting with the MR-SoftWrist during an fMRI scan. Additionally, the end-effector frame of the robot is shown, which matches the anatomical axes of the subject's wrist.

MR-compatible (i.e. it will not interfere with the quality of scanned images or have its own performance affected by the fMRI process). To be MR-safe, no ferrous components should be used and conductive loops that couple to the switching gradients or to the RF pulses should be avoided. Such loops can cause heating and burn the skin of the subject. In contrast, being MR-compatible is more complicated. Some of the factors that play a role in MR-compatibility are the amount of metallic and electrically active components, especially those near the region of interest, i.e. the brain, or those that move through magnetic field lines. Moving electrically active or metallic components can produce electromagnetic interference [11]. The robot is not the only factor potentially involved in image degradation. The task itself should be carefully selected, since the quality of fMRI images is substantially degraded by head movements and displacement of body mass in proximity of the region of interest [12]. Distal arm movements are more suited to fMRI studies, since it has been shown that shoulder and elbow movements result in much larger head motions than those involving the wrist [13]. Despite this fact, studies have mainly focused on sweeping arm movements [11], [14] which may be a result of the challenges to create a multi-DOF haptic device targeting the wrist. Also complicating matters, subjects typically lie supine on the scanner bed inside a 60-70 cm scanner bore, making it challenging to fit both the robot and person inside the same small area.

Although single-DOF haptic interfaces [15] are attractive because of their simplicity and capability to study isolated joint movements, multi-DOF haptic interfaces offer a broader range of possibilities for neuroscience purposes, studying, for example, adaptation to lateral force fields [10], or redundant tasks [16]. However, the design of multi-DOF MR-compatible robots with accurate kinesthetic feedback capabilities has so far proved challenging. Previous approaches to multi-DOF MR-compatible haptic devices have included a 2DOF hydraulic system [17], a 3DOF system using shielded electromagnetic motors [18], and a proposed design for a 6DOF device using ultrasonic motors (USMs) [19]. All of these devices are limited in terms of position measuring accuracy since they do not measure joint movement directly. Additionally, the use of hydraulic actuation [17] or long carbon fiber rods to connect the device with the user [18] limit force

bandwidth. Finally, the latter two functional devices are limited by the fact that they are intended for use with unconstrained arm movements, an intrinsically non MR-compatible task.

To address these constraints, we have recently developed an MR-compatible 2DOF wrist robot, the MR-SoftWrist [20], enabled by MR-compatible USM actuation with compliant force feedback [21]. The MR-SoftWrist is the first MR-compatible multi-DOF haptic wrist robot, and is capable of measuring and supporting wrist motions during fMRI. The MR-SoftWrist is placed at the edge of the MR machine's scanner bore and extends its links to a wrist ring end effector which connects the device to the user's wrist for kinesthetic feedback.

In this paper, we characterize the dynamic interaction control capabilities of the MR-SoftWrist and present a single subject case study showing applications of the robot in motor control studies (Fig. 1). We substantially extend our previous work, presenting a complete dynamic characterization and validation of the MR-SoftWrist. Moreover, we validate the device capabilities, by presenting the results of a case study where a user interacts with the robot during fMRI through three control modes in a semicircular arc pointing task with the wrist. To the best of our knowledge, this is the first contribution presenting a complete dynamic characterization and validation of a multi-DOF force-feedback robot for motor control experiments during fMRI.

## II. MR-SOFTWRIST

In the following section, we provide an overview of the robot used in this study, the MR-SoftWrist, describing its kinematic structure, components, and properties. The MR-SoftWrist interacts with a user's wrist instead of more proximal limbs as done in [14], [17], [18], which should reduce head movements and moving body mass during scanning, thus improving fMRI image quality [12]. General design requirements for the manipulator are capability of position, low-impedance, and force-source control modes [22], [23]. In our previous work [21] we proposed an actuation approach that uses USMs in a parallel kinematic architecture. We determined that the achievable circular workspace for wrist FE and radial/ulnar deviation (RUD) is 20 deg, and that 1.5 N-m of continuous torque output can be provided.

TABLE I  
MR-SOFTWRIST SPECIFICATIONS

Joint	MR-SoftWrist						ADL	
	$k$ [N-mm/deg]	$\theta_{res}$ [deg]	$\dot{\theta}_{max}$ [deg/s]	$\theta_{range}$ [deg]	$\tau_{res}$ [N-mm]	$\tau_{max}$ [N-m]	$\theta_{range}$ [deg]	$\tau_{max}$ [N-m]
FE	370	0.02	115	40	$9 \cdot 10^{-3}$	2.80	115	0.35
RUD	370	0.02	115	40	$8 \cdot 10^{-3}$	2.45	70	0.35

### A. Mechanical Design

A parallel design was pursued to achieve high structural rigidity, velocity, and torque output with low inertia as compared to an equivalent serial manipulator. Additionally, the parallel design places the actuators on a stationary base frame, reducing potential imaging artifacts from active electrical components moving in the scanner’s magnetic field. A three revolute-prismatic-spherical kinematic structure was chosen, which consists of a base ring and three legs, each of which include a revolute, prismatic (actuated), and spherical joint [24]. Each spherical joint is mounted equidistantly on a wrist ring, which serves as the robot’s end-effector. The mechanism provides 3DOFs corresponding to  $z_c$  (the platform height),  $\theta_{FE}$  (wrist FE, a rotation about  $\hat{x}$ ), and  $\theta_{RUD}$  (wrist RUD, a rotation about  $\hat{y}$ ) (see Fig. 1). A design was pursued such that the user’s hand moves in the space between the base and wrist rings. Although  $z_c$  is a DOF of the device, it is fixed through control to provide alignment to the subject’s wrist anatomical axes. As a consequence, when coupled to a subject, the robot task space effectively reduces to the 2D space defined by  $\theta_{FE}$  and  $\theta_{RUD}$ . With a suitable value for  $z_c$ , this solution places the actuators at the edge of the scanner bore, which is beneficial for the device’s performance and for avoiding interference with scanned images. The device is therefore in its nominal configuration when  $\theta_{FE} = \theta_{RUD} = 0$  and  $z_c = z_{c,nom}$ .

A relevant measure of the robot workspace size is the radius of the circle inscribed within admissible solutions in the 2D task space (for  $\theta_{FE}$  and  $\theta_{RUD}$ ) defined by the selection of a specific  $z_{c,nom}$  value. By carefully selecting the base platform ( $R$ ) and end effector ( $r$ ) radii, a 20 deg workspace radius was achieved such that the user’s hand would not make contact with the device within this workspace and that required each link to travel about 40 mm. To accommodate users of varying size, linear bearings with 75 mm of travel were selected to allow for the desired 20 deg workspace radius to be achieved for a variety of  $z_c$  values. The chosen structural values were 255 mm for  $z_{c,nom}$  (corresponding to 274 mm nominal link lengths), 168 mm for  $R$  and 67 mm for  $r$ . For more details on the design of the device, readers are referred to our previous work [20].

### B. Mechanical Properties

For the torque output of the MR-SoftWrist, the limiting factor is the maximum force on the springs (25 N), resulting in a torque of 138 N-mm on the USM, almost four times less than its maximum continuous torque of 0.5 N-m. Depending on the configuration of the device, its maximum velocity and torque output varies. Through analysis described in [20], the maximum torque and velocity limits of the device were computed

for  $z_{c,nom}$  while varying the task space coordinates within the device’s 20 degree circular workspace. The MR-SoftWrist’s specifications are presented in Table I, which includes the device’s stiffness coefficients and workspace radius, as well as its velocity and torque limits and respective resolutions. As a comparison, wrist workspace and torque values for activities of daily living (ADL) are given using values obtained from [25]. The task space stiffness of the MR-SoftWrist,  $k$ , is about 7 times higher than the highest stiffness of the human wrist for combined RUD and FE rotations, which is estimated in several studies such as in [26]. The task space stiffness value has been selected by trading off position control bandwidth during interaction with a passive subject (which increases for increasing stiffness values) with force measurement resolution (which instead decreases for increasing stiffness values.)

### C. Components

The MR-SoftWrist is a co-located robot, requiring all components to be MR-compatible. Due to its high rigidity and light-weight properties, Delrin was selected for all structural components. Brass screws were selected for securing all components due to their low magnetic susceptibility and high strength. The actuated prismatic joints are linear series elastic actuators [21] composed of a rotary USM (Shinsei Corp. USR60-E3NT with the D6060E/24V motor driver) with an 11.5 mm diameter pulley, secured to the motor shaft through a brass set screw, connected to custom brass extension springs (1.9 N/mm) through a nylon cable transmission. The two springs are connected at each end of a slider through nylon eyebolts which are also used for pre-tensioning the springs. The springs are placed in parallel to each other but in series between the USM and load. Load deflection is measured through a linear optical encoder (US Digital EM1-0-500-I). The slider is supported by brass housed linear bearings with ceramic balls and titanium shafts (Del-Tron Precision Inc. S2-3-NMS-Brass). The actuated prismatic joints are supported by two ceramic radial ball bearings which are mounted on a brass shoulder screw secured to the base. Since no commercial MR-compatible spherical joint exists, the spherical joints were approximated through a revolute-universal-revolute kinematic chain. Ceramic ball bearings were used for the revolute joints while the universal joints (Ondrives size 6 plastic universal joint) are made of brass and Delrin.

In addition to its mechanical components, an important feature of the MR-SoftWrist is the shielding and filtering of its motor and encoder lines. The MR-SoftWrist is comprised of several electrically active components – six optical encoders and three USMs (voltages on the order of 200 V at 40-45 kHz). Operation of such elements during imaging can introduce elec-

tromagnetic interference, if the signal is not filtered properly to a ground reference, such as the one provided by the scanner penetration panel. In an effort to reduce electromagnetic interference introduced by these active components, tripolar twisted-pair shielded cable with an additional outer shield was used for encoder lines, and the load optical encoder cases were wrapped with aluminum foil. The USMs were wrapped in aluminum foil along with their respective encoders. The shield of the load optical encoders was connected to their respective foil on one side and to the penetration panel on the other to ensure a low-impedance path to ground, attenuating the noise generated by active components through a Faraday cage. To ensure decoupling of the signal references and to avoid introducing noise in the scanner room coming from the unshielded control room, the motor signal and encoder lines were low-pass filtered using 1300 pF and 5600 pF capacitive filters respectively. The filter frames were grounded by the penetration panel.

### III. DEVICE DYNAMIC CHARACTERIZATION

A variety of experiments are presented which thoroughly characterize the dynamic performance of the MR-SoftWrist. The device's control scheme is presented, along with experiments evaluating its position control and force measurement accuracy. These experiments warrant use of the device as a kinesthetic feedback machine, capable of rendering virtual environments such as a transparent mode, with null displayed force, to different values of virtual stiffness, to unstable diverging environments.

#### A. Kinesthetic Feedback Capabilities

The MR-SoftWrist can be controlled to render a variety of virtual environments through impedance control as shown in Fig. 2, using a low-level cascaded force-velocity control scheme typical of series elastic actuators (SEAs) [27]. The implementation of the low level force controller, labeled as "JS SEA Force control" in Fig. 2, on the USMs is described in detail in [21]. Control of the MR-SoftWrist is performed through real-time software in a Matlab-Simulink model communicating with Quanser's Q8 USB board at a 1 kHz loop rate. The device Jacobian  $\mathbf{J}$  is obtained through the formulation found in [28]. In [28] the Jacobian is given as  $\rho(\mathbf{q}')$ , a matrix relating task space to joint space velocities, where  $\mathbf{q}'$  is a vector including all of the device's generalized coordinates (12 for the MR-SoftWrist). The forward kinematics (FK) of the device are acquired through the method discussed in [29]. This solution seeks to find a coordinate transformation  $\mathbf{q}' = \sigma(\mathbf{q})$  between the independent and generalized coordinates. This is accomplished through an iterative solution which guarantees the existence of  $\sigma(\mathbf{q})$  and can be computed in real-time. The iterative solution is formulated by deriving the nine kinematic constraint equations of the MR-SoftWrist, with a vector equation (three scalar equations) derived for each of the robot legs, as is standard in parallel manipulators.

#### B. Position Control Accuracy

To illustrate the ability of the device to track reference trajectories, the device was commanded to track a 20 degree

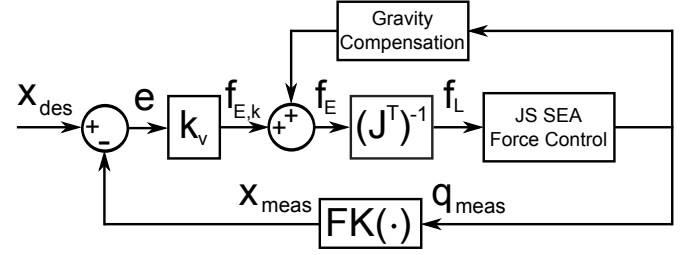


Fig. 2. Block diagram of task space impedance control, in this case the impedance is a virtual spring, for the MR-SoftWrist. Desired task space position ( $\mathbf{x}_{des}$ ), measured task space position ( $\mathbf{x}_{meas}$ ), task space position error ( $\mathbf{e}$ ), task space virtual spring stiffness ( $\mathbf{k}_v$ ), force error without considering gravitational loading ( $\mathbf{f}_{E,k}$ ), gravity compensation model shown in Fig. S2, task space forces and torques ( $\mathbf{f}_E$ ), Jacobian ( $\mathbf{J}$ ), joint space load forces ( $\mathbf{f}_L$ ), force control performed at the joint space level as in [21], measured joint space position ( $\mathbf{q}_{meas}$ ), and forward kinematics ( $\text{FK}(\cdot)$ ). For details on the gravity compensation scheme, see Section B in the Supplementary Materials.

circle in 2D task space coordinates ( $\theta_{FE}$  and  $\theta_{RUD}$ ) through a sinusoidal reference oscillating at 0.4 Hz (see Fig. S1 in the Supplementary Materials). This experiment also shows that the device meets the desired workspace while achieving good position tracking capabilities, resulting in a root mean square error of 2.25 deg and a maximum error of 3.45 deg in tracking either DOF.

#### C. Force Measuring Accuracy

As the MR-SoftWrist acquires force measurements in joint space coordinates, the accuracy of task space interaction force/torque measurements can be compromised by non-ideal transmission elements. To estimate the accuracy of such task space force measurements, a six axis force/torque transducer (ATI Nano17 SI-25-0.25) was used as a ground truth reading. The ATI Nano17 was mounted on a handle attached to the wrist ring. In this way, the loading path of forces and torques applied by a user would propagate through the ATI Nano17 before being transferred through the wrist ring, spherical joints, and then the springs. Measurements of the ATI Nano17 were transformed to task space coordinates through a force-torque transform based off of distance and angular offsets obtained from a CAD rendering of the device. These measurements were compared with task space force measurements of the MR-SoftWrist by multiplying joint space force readings (from the linear springs) by the transpose of the device Jacobian.

To estimate the force measuring accuracy of the device in its neutral configuration, a human experimenter applied quasi-static loads on the handle by grasping it and pushing/pulling in various directions with roughly sinusoidal profiles. In this experiment, the robot was blocked, so the springs are expected to measure the force applied to the MR-SoftWrist handle. Forces up to 8 N were applied in the  $\hat{z}$  DOF ( $F_z$ ) and torques of up to 460 N-mm and 630 N-mm were applied to the FE ( $\tau_{FE}$ ) and RUD ( $\tau_{RUD}$ ) DOFs respectively. The comparison of force measurements over a 10 s time period can be seen in Fig. 3 which resulted in mean errors of 0.3 N, 17 N-mm, and 34 N-mm for  $F_z$ ,  $\tau_{FE}$ , and  $\tau_{RUD}$  respectively. Given the accuracy in force measurements, reported torque values in future experiments will be those derived from spring estimates. A

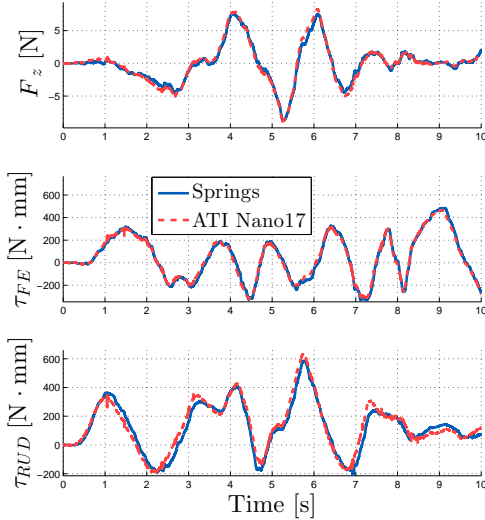


Fig. 3. Resulting task space force and torques from an experimenter applying quasistatic loads on the device’s handle. Force measurements from the springs were transformed with the Jacobian to task space variables while measurements from the ATI Nano17’s sensor frame were transformed to task space variables via a force-torque transform.

possible explanation for the small error in force measurement is the compliance of the plastic structural components, as well as the play and friction in the universal joints.

#### D. Zero Force Control

Interaction control of the device was realized with the task space impedance control scheme shown in Fig. 2. To implement zero force control, the virtual spring constant ( $\mathbf{k}_v$ ) was set to the null vector, resulting in the desired task space torques being equal to zero. The low-level force controller presented in [21] was implemented on each actuation module. Such a cascaded force-velocity series elastic actuator controller contains a proportional gain for the outer force loop that determines the control effort based on force measurement error. When a user attempts to make transparent movements during zero force control, they feel a damping force which is inversely proportional to this inner loop proportional gain. This gain can be experimentally tuned so that it is high enough to provide a transparent environment without the risk of creating an unstable system. There is also a deadband of 0.2 N on joint space force measurements since the USM cannot regulate velocities under 14 rpm. If there was no deadband present, the device would enter a limit cycle due to its low-velocity nonlinearity. To see how the zero force controller improves the backdrivability of the MR-SoftWrist, please see the movie clip “Zero Force Demonstration” in the Supplementary Materials.

Three separate zero force control experiments were performed for three different types of unidimensional trajectories  $\theta_L(t)$ , i.e. linear trajectories along the  $\theta_{FE}$ ,  $\theta_{RUD}$  axes, and circular movements in the robot workspace, defined by angle  $\phi = \text{atan2}(\theta_{RUD}, \theta_{FE})$ , using zero-force control with gravity compensation. A user performed sinusoidal movements of varying velocity and frequency with velocities at the MR-SoftWrist’s limits ( $\sim 100$  deg/s). The results of these exper-

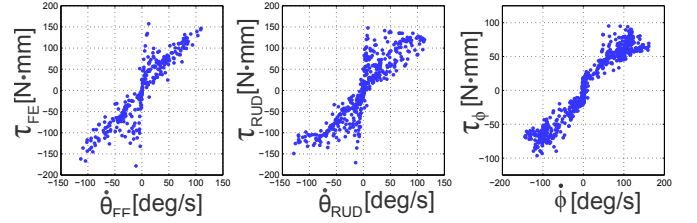


Fig. 4. Experimental validation of zero force control for FE, RUD, and circular movements. The damping force is inversely proportional to the proportional gain at the joint space force control level. The data has been down sampled to 50 Hz for visualization.

iments can be seen in Fig. 4. A fit was performed separately for each experiment’s coordinates with the model

$$\tau_L = I\ddot{\theta}_L + b\dot{\theta}_L + \tau_c \text{sign}(\dot{\theta}_L) \quad (1)$$

where  $\tau_L$  is the applied load torque as measured by the springs,  $I$  the device inertia,  $b$  the perceived damping, and  $\tau_c$  the perceived Coulomb friction. A multiple linear regression was performed which gave estimates of  $I$ ,  $b$ , and  $\tau_c$  for each coordinate. The values are presented in Table II. Plots of velocity versus torque for the three experiments can be seen in Fig. 4, demonstrating that at low velocities the user perceives a Coulomb friction force, while at higher velocities the damping force dominates. There is an additional inertial effect from the mass of the legs and end effector that can be noticed at intermediate velocities from the deviation of torques from the straight line portion of the data. It should be noted that the main cause of the perceived Coulomb friction is the use of the deadband on joint space force measurements, required to compensate the USM low-velocity nonlinearity [21].

#### E. Rendering Virtual Stiffnesses

To render virtual stiffnesses, the MR-SoftWrist uses the control structure from Fig. 2 with the choice of  $\mathbf{k}_v$  as a symmetric, positive semidefinite  $3 \times 3$  matrix. Two sets of experiments were performed to evaluate rendering virtual stiffnesses with the MR-SoftWrist. Both tests were performed for either wrist FE or RUD where one DOF (FE or RUD, respectively) was commanded to display a virtual stiffness, while the other two (including  $z_c$ ) were commanded to display zero force. In the first experiment, a static interaction test, an experimenter applied quasi-static loads through the device’s handle for various virtual stiffnesses in the direction of the desired DOF. This experiment evaluated how well the device can track desired force trajectories for varying impedances. In the second experiment, to characterize the device’s dynamic range, an experimenter applied sinusoidal motions of varying

TABLE II  
ZERO FORCE CONTROL PARAMETERS

	$I$ [kg · m <sup>2</sup> ]	$b$ [N·mm·s/deg]	$\tau_c$ [N·mm]	$R^2$
FE	0.0016	1.25	15	0.84
RUD	0.0018	1.14	15	0.87
$\phi$	0.0005	0.58	5.4	0.93

frequency, with frequency content up to 5-10 Hz, for the same varying impedance values. Estimates of the virtual stiffness transfer function  $K_v(f) = \frac{T_L(f)}{\Theta_L(f)}$  relating the Fourier transform of output torque ( $T_L(f)$ ) to the Fourier transform of input position ( $\Theta_L(f)$ ) were obtained using the Matlab function `tfestimate` for each experiment. The results of both experiments are presented in Fig. 5. Defining bandwidth as the frequency range for which the ratio of virtual to desired spring stiffness is within  $\pm 3$  dB, the device has a minimum bandwidth of 5.5 Hz which occurs for the lowest virtual stiffness for RUD.

#### IV. SYSTEM VALIDATION

A set of experiments was performed to determine if the MR-SoftWrist can function safely inside the MRI room without distorting fMRI images, involving both phantom scans and experiments with human subjects. For the experiments involving human subjects, informed consent was obtained under a protocol approved by the Rice University Institutional Review Board (protocol no. 668026). The validation experiments conducted with healthy subjects during fMRI sought to establish the possibility of using the MR-SoftWrist to replicate motor control experiments (such as in [30], [31]) by interacting with a user's wrist with accurate kinesthetic feedback while not interfering with fMRI images.

##### A. MR-Compatibility Tests

MR-compatibility scans were conducted via experiments on a gel phantom as reported extensively in a companion paper [32], where we quantified the increase of intrinsic signal fluctuations introduced by the MR-SoftWrist to be equal to 1.8% of the baseline value, and established the increase to be significant at the  $p < 0.05$  level.

Based on the phantom experiment result, we sought to quantify its impact on the quality of functional images acquired during fMRI both via a numerical simulation and via experiments with a human subject. Via numerical analysis, we estimated that loss in fMRI contrast, resulting from the increase in noise occurring in the presence of the robot, could be compensated by simply increasing the total duration of a given fMRI experiment by 3%, or approximately 6 s for a 3.5 min long experiment [32]. In a standard block-design experiment with a human subject, we did not find any significant effect introduced by the operation of the robot in both the size and amplitude of activation measured for a representative sensorimotor experiment. Both experiments, presented in detail in [32], confirm that the increase in signal fluctuations introduced by the MR-SoftWrist is not sufficient to significantly degrade the quality of functional images measured during operation of the robot.

##### B. Single Subject Case Study

We conducted a case study with one healthy subject involving a semicircular arc pointing task under controlled kinesthetic feedback during fMRI (see Fig. 1). The specific goal of the case study was to validate the device as an MR-compatible haptic interface for wrist sensorimotor protocols

with kinesthetic feedback, by demonstrating the possibility of computer-controlled force display to elicit distinguishable kinetics and neural response without image artifacts due to head movements and/or noise.

1) *Methods*: A healthy male subject (25 yr) was involved in an fMRI experiment consisting of a 2DOF wrist circular arc pointing task, modeled after the task presented in [5], requiring wrist FE (angle mapped on the horizontal axis) and RUD, along a circular trajectory with radius  $\rho = 15$  deg. The task involved pointing from an east target ( $\theta_{FE} = \rho, \theta_{RUD} = 0$ ) to a west target ( $\theta_{FE} = -\rho, \theta_{RUD} = 0$  deg) (see Fig. 6 top, left). During the pointing task, the subject received online visual feedback; movement initiation and direction were triggered by visual display of a ghost cursor, which moved along the circle in either a clockwise or counterclockwise direction, reaching the target  $T_d = 3$  s after departure. After the subject reached the target and maintained his position over the target for 0.5 s, the ghost cursor started movements toward the next target, along a circular trajectory that was calculated from polar coordinates with constant distance  $\rho$  and angle  $\phi(t)$  determined from a minimum-jerk trajectory with extent 180 deg. Guide lines were displayed around the desired trajectory, and the subject was instructed to try to remain inside them during the circular pointing task and to reach the target before the ghost cursor, moving along the same direction (either clockwise or counterclockwise).

During the experiment, the MR-SoftWrist was controlled with the task space impedance controller shown in Fig. 2, with  $\mathbf{x}_{des}$  defined at each iteration as the point minimizing the Euclidean distance in the task space between the measured position  $\mathbf{x}$  and the circle with radius  $\rho$ , obtained through iterative numerical optimization. After calculation of  $\mathbf{x}_{des}$ , the task space desired force vector  $\mathbf{f}_{E,k} = k_v(\mathbf{x}_{des} - \mathbf{x})$  (with  $k_v$  scalar) was projected along the normal direction to the circle and applied via the task space force controller shown in Fig. 2. Three modes were implemented and tested in the pilot study: *i*) zero force (ZF) mode, with  $k_v = 0$ ; *ii*) path control (PC) mode, with  $k_v > 0$ ; *iii*) error augmentation (EA) mode, with  $k_v < 0$ . Constants of  $k_v = -30$  N·mm/deg and  $k_v = 230$  N·mm/deg were chosen for the EA and PC modes respectively. The gain constants were manually tuned to result in noticeable and measurable task space assistance/perturbation forces within conservative safety and stability margins. To prevent possible hardware failures deriving from task instabilities, force output generated in the EA mode was also limited to 100 N·mm. In the Supplementary Materials, three multimedia MOV format movie clips have been provided of a user interacting with the MR-SoftWrist during these three control modes.

After a training session to familiarize themselves with the robot and its control modes (roughly 30 min in a side lab outside the scanner), the subject executed the wrist pointing task during fMRI in repeated block design experiments (one per each control mode). Each experiment consisted of the alternation of visual control (VC) blocks and active blocks. In the VC blocks, the ghost cursor was moving and the subject was informed by a "STOP" message appearing at the beginning of the block to follow only visually the movements of the ghost cursor. A movie clip of the "STOP" block has

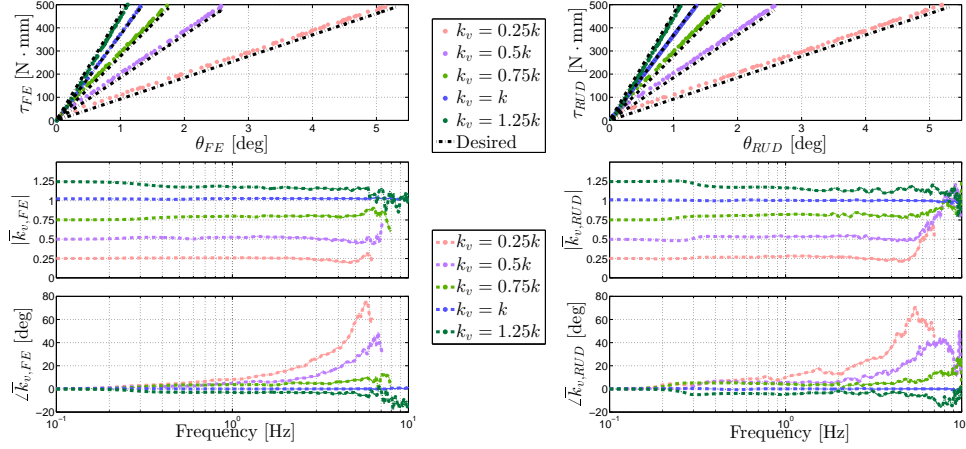


Fig. 5. Characterization of the task space stiffness control of the MR-SoftWrist, as described by the torque vs. angular displacement plots (top) for FE (left) and RUD (right) under the application of slowly increased loading; and by Bode plots of the virtual stiffness transfer function  $\bar{K}_v(s) = \frac{K_v(s)}{k}$  under dynamic manual perturbations. Experiments at different values of commanded virtual stiffness  $k_v$  are conducted, and values are reported as a function of the natural manipulator stiffness in task space coordinates  $k$ . The Bode plots only show estimated transfer function values with coherence values greater than 0.8.

been provided in the Supplementary Materials. In the active block, the subject was instead asked to perform circular wrist pointing movements. Each block consisted of six repetitions, each with random direction, with a minimum block duration of 21 s (actual block durations could vary depending on the time required for the subject to complete the movement). Each experiment switched between seven VC blocks and six active blocks, for a total experiment duration of  $305 \pm 5$  s. During the functional experiment, a standard echo-planar imaging sequence was used (voxel size: 2.5 mm isotropic - no gaps, image size: 80x80 px, no. slices: 42, scanned volume: box with edges 200x200x105 mm, flip angle=78 deg, TE=35 ms, TR=2000 ms, pixel bandwidth=1453 Hz/pixel) covering the entire cerebrum and the superior part of the cerebellum. After the functional experiment, a high-resolution structural scan (magnetization-prepared rapid acquisition with gradient echo (MPRAGE), voxel size: 1 mm isotropic - no gaps, scanned volume: box with edges 256x256x176 mm, flip angle=8 deg, TE=3.03 ms, pixel bandwidth=130 Hz/pixel) was conducted to allow registration of the functional images.

2) *Data Analysis - Robot*: Kinematic and force data were collected continuously during the experiments and logged at 50 Hz. A scalar error value  $e$  was defined at each time sample as the distance between the current position and the desired trajectory  $e(i) = |\mathbf{x}(i) - \mathbf{x}_{\text{des}}(i)|$ ; for each movement  $k$  (composed of  $M$  samples) an average error  $e_k = \sum_i^M \frac{1}{M} e(i)$  was defined and used for statistical analysis. Interaction force values were similarly measured from spring deflections, converted to task space torques, and averaged for each movement for comparison between different experimental conditions. The estimated task space interaction forces were projected along the tangent to the circle measured by the current point  $\mathbf{x}_{\text{des}}(i)$ , which enabled distinguishing between lateral perturbation forces  $F_{\text{lat}}$ , normal to the desired trajectory, and resistance forces  $F_t$ , along the desired trajectory.

3) *Data Analysis - fMRI*: The images acquired during the three block design experiments were analyzed with a standard fMRI processing batch, including realignment (to

the first image, using SPM8 – Wellcome Department of Imaging Neuroscience, London, UK – realignment function, with options quality = 95%, separation 2.5 mm), coregistration to the structural MPRAGE (using the SPM8 coregistration function with the normalize mutual information option, with progressively decreasing separation of 4 mm, 2 mm and 1 mm), spatial normalization (using SPM8 preset values), smoothing with an isotropic Gaussian filter (full width half maximum 8 mm), and high-pass filtering (time constant=128 s). A general linear model was constructed for each experimental condition, using the block variable (stimulus on/off), convolved with the SPM8 canonical hemodynamic response function, as the regressor of interest, and adding head motion parameters estimated through realignment as nuisance regressors. To determine differential activation in response to different haptic environments, the EA and ZF runs were concatenated in time and underwent the same pre-processing steps, with the exception of high-pass filtering, which was disabled for the analysis including concatenated data. A second general linear model was constructed, using the block variables (stimulus on/off) convolved with the canonical hemodynamic response function as regressors of interest, and using constant and linearly increasing regressors to account for the non-continuous acquired data. Model estimation yielded  $t$ -maps for the first three general linear models, one for each experimental condition relative to baseline (Active>VC), and estimation of the second general linear model yielded parametric maps for the difference between activation in the two experimental conditions (EA-ZF>0). Using SPM8 correction for multiple comparisons (family wise error correction at  $p < 0.05$ ), the voxel-level false discovery rate thresholded  $t$  score for the whole brain analysis was  $4.8 \pm 0.1$ .

4) *Results - Robot*: During the semicircular pointing task conducted in the scanner, the MR-SoftWrist was capable of implementing kinesthetic feedback to manipulate error depending on the selected control mode ( $e_{EA} = 1.7 \pm 0.6$  deg,  $e_{ZF} = 0.9 \pm 0.3$  deg,  $e_{PC} = 0.3 \pm 0.1$  deg, mean  $\pm$  standard deviation) (see Fig. 6 top,right), with all paired comparisons

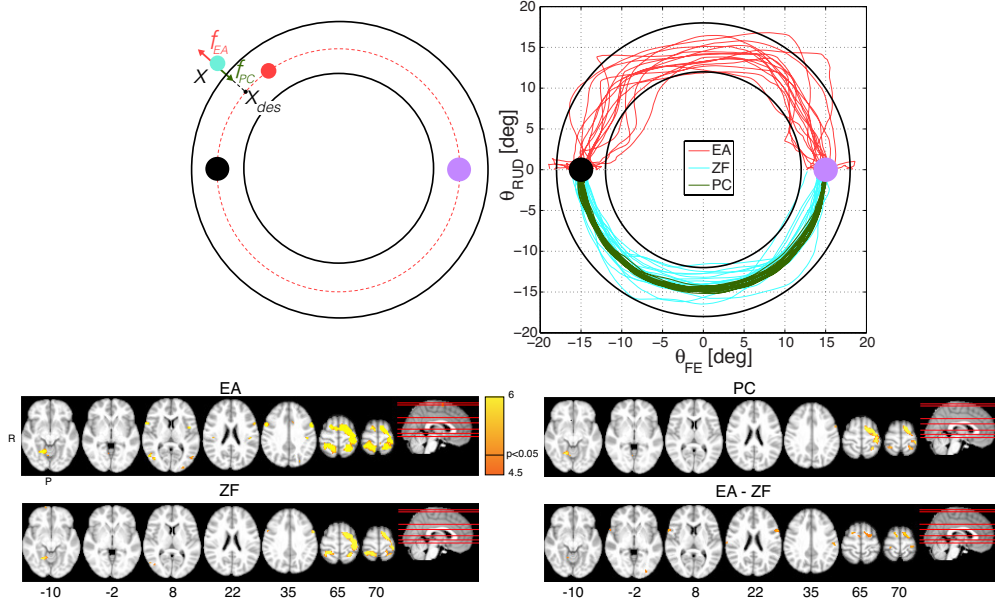


Fig. 6. Pilot study results. (top, left) GUI of the force feedback schematic for the circular wrist pointing task. The subject position ( $x$ ) is displayed with the cyan cursor, and movement direction is visually cued with the red ghost cursor towards the correct target. The force feedback controller, shown in Fig. 2, is implemented, with  $x_{des}$  being the nearest point along the circular trajectory. With positive  $k_v$ , the robot implements path control (PC), while with negative  $k_v$  the robot implements error augmentation (EA). When  $k_v = 0$  the robot implements the zero force (ZF) mode (colors in this image differ from the experiment for improved quality in grayscale print). (top, right) Kinematics measured in the three different control modes, during the pilot study experiment. EA is only shown in the top portion, and ZF and PC are shown only in the lower portion. (bottom) Task related activation for the Active>Visual Control conditions (EA, PC and ZF), and for the contrast between EA and ZF conditions (EA-ZF). Statistical parametric maps are overlaid on the standard Montreal Neurological Institute 152 template, as axial multislices, cut at  $z$  values labeled below the images. Note that  $t$  values higher than the colormap maximum are saturated to the highest intensity values.

(one-tailed  $t$  test, dof= 70) rejecting the null hypothesis with high statistical significance ( $p < 0.001$ ). Error manipulation was achieved through regulation of task space interaction force in the perpendicular direction to the task ( $F_{lat,EA}=40\pm 12$  N·mm,  $F_{lat,ZF}=10\pm 2$  N·mm,  $F_{lat,PC}=22\pm 8$  N·mm), with all paired comparisons for the  $F_{lat}$  values significant at  $p < 0.001$ . In contrast, differences in resistance force displayed along the tangential task direction were minimal ( $F_{t,EA}=41\pm 2$  N·mm,  $F_{t,ZF}=43\pm 2$  N·mm,  $F_{t,PC}=44\pm 3$  N·mm), and mostly explained by variability in tangential velocity among different control modes that results in slightly different interaction force values (refer to the zero force behavior shown in Fig. 4 right).

5) *Results - fMRI*: The total head displacement during the experiments, as estimated from image realignment parameters, was within 1 mm and 1 deg in all conditions. No large artifacts (i.e. volume distortions or RF noise lines) could be detected from visual inspection of the scanned volumes. Task-related activation maps revealed activation in the contralateral primary motor cortex (M1), and bilaterally in the somatosensory (SS) cortex (including Brodmann Areas BA1, BA2 and BA3). Activation in the premotor cortex (PM) was bilateral in the EA mode, but only contralateral in the ZF and PC modes (see Fig. 6 bottom). Common activation in the different experimental conditions was measured also in the superior portion of ipsilateral cerebellum vermis V (only the superior 20% of the cerebellum was included in the functional imaging volume). The contrast between activation in the EA and ZF conditions revealed areas with higher activation in the EA mode relative

to the ZF mode, which included bilateral portions of the PM and SS cortex, and bilateral BA44 (part of Broca's area).

## V. DISCUSSION AND CONCLUSIONS

The MR-SoftWrist is a novel MR-compatible wrist robot capable of accurate kinesthetic feedback during 2DOF wrist pointing movements executed during fMRI. In this paper, we have presented a detailed dynamic characterization of its capability to display virtual environments via kinesthetic feedback, and validated the entire system in a single subject case study involving semicircular arc pointing with the wrist during fMRI under convergent, divergent, and null force fields.

The development of an accurate and high-bandwidth kinesthetic feedback robot suitable for operation during fMRI required investigation of non-standard mechatronic design practices. The MR-SoftWrist uses a parallel architecture, placing its three actuators on a stationary base frame, as well as providing increased structural rigidity and increased torque and speed output compared to a serial design. To guarantee MR-compatibility, the MR-SoftWrist is actuated via non-backdrivable piezoelectric ultrasonic motors, and interaction control is achieved via force control based on the measurement of the linear deflection of three compliant elements. To our knowledge, the MR-SoftWrist is the first parallel manipulator employing non-backdrivable actuators and a compliant transmission to render task space virtual impedances. With its workspace including wrist FE and RUD rotations in a circle with a 20 deg radius, and capability for 1.5 N·m of torque

around both wrist axes, the device is suitable for investigating wrist sensorimotor protocols under force feedback during fMRI.

Position control was demonstrated for a sinusoidal trajectory covering the entire 2D workspace, oscillating at a frequency of 0.4 Hz. The root mean square error was 2.25 deg while the maximum error was 3.45 deg in tracking either DOF. Although this error is large compared to the performance of non MR-compatible rehabilitation robots [33], it is a result of the use of series elastic actuation, which facilitates interaction control, but does not allow high position control bandwidth and accuracy. Since position control would mainly be used for playing back user motions in visual- and proprioception-controlled experiments, the limitation in position control accuracy is justified by the requirement of achieving accurate task space impedance control. Torque measurement accuracy of the MR-SoftWrist was evaluated in a static test, yielding mean force estimate errors of 17 N-mm and 34 N-mm for  $\tau_{FE}$  and  $\tau_{RUD}$  respectively. This test shows that the MR-SoftWrist is capable of measuring user interaction torques accurately within the series elastic architecture, validating the use of the device as an accurate force measuring device for haptic fMRI experiments.

The ability of the MR-SoftWrist to display a transparent mode was evaluated in three experiments: one for each DOF and one for a representative task (in this case wrist pointing along a circular trajectory in FE and RUD coordinates). The maximum backdrivability torque for wrist FE and RUD was found to be approximately 150 N-mm at 100 deg/s in each case. Estimated Coulomb friction from each DOF were the same (15 N-mm) while other parameters were similar, i.e. inertia estimates of 0.0016 and 0.0018 kg-m<sup>2</sup> and damping estimates of 1.25 and 1.14 N-mm-s/deg for FE and RUD respectively. The MR-SoftWrist's maximum backdrivability torque and inertia estimates are almost identical to those of the wrist module of the MIT-MANUS [34]. Additionally, the maximum interaction force of 150 N-mm felt by the user is only 10% of the maximum output torque.

Impedance control of the device was evaluated by validating its ability to display a range of virtual stiffnesses for both static and dynamic cases. Static experiments showed accurate tracking, while dynamic experiments revealed that the device is capable of achieving at least 5.5 Hz of impedance control bandwidth. This is more than sufficient for the range of 2-5 Hz for human movements [35] and far exceeds the approximately 1 Hz position control bandwidth of previous MR-compatible force feedback haptic interfaces [15]. Additionally, the device can stably render impedances higher than those of the device's physical impedance, although these impedances are not passive [27], [36].

In addition to quantitative MR-compatibility analysis via phantom and human subject experiments [32], we have here validated the MR-SoftWrist in a case study with a single healthy subject, demonstrating the capability of the device to apply force feedback to elicit distinguishable kinetic and neural response. The pilot validation study demonstrated the capability of simultaneous acquisition of functional images during interaction with the MR-SoftWrist as demonstrated by

the limited head movements. Activation maps were determined for different control modalities, including path control (PC), zero force (ZF) and error augmentation (EA). Comparison of the activation maps showed that activation in the premotor cortex (PM) was bilateral in the EA mode, but only contralateral in the ZF and PC modes, suggesting a potential involvement of the ipsilateral PM with increased task difficulty. The contrast between activation in the EA and ZF conditions revealed areas with higher activation in the EA mode relative to the ZF mode, which included bilateral portions of the PM and SS cortex, and bilateral BA44 (part of Broca's area), suggesting a role for BA44 in processing and responding to force perturbations. This is in agreement with previous models suggesting the involvement of Broca's area in hand movement, and suggesting that Broca's area might have a role in linking forward and inverse models [37]. However, this result might be dependent on the specific task implemented in this study, where a ghost cursor was continuously presented in the visual display, introducing some form of action imitation in the task, and potentially increasing the involvement of Broca's area [38]. Significant activation was observed in the EA mode also in parts of the contralateral cerebellum, confirming models predicting increased cerebellar involvement in construction and processing of internal models and tool use [39]. These functional neuroimaging results indicate capability of generation of experimentally-controllable activation maps in response to haptic environments, but the results of this study are not at all meant to provide any findings on the neural correlates of robot-assisted motor control, given the inclusion of only one subject in the analysis.

The MR-SoftWrist is a new tool that can be useful to study motor learning under haptic guidance. The device can control multi-DOF movements directly unlike most other MR-compatible robots, which control unconstrained movements through an end effector design [14], [18], [40]. Additionally, the MR-SoftWrist interacts with the wrist and thus does not induce significant head motion, which has shown to be a significant issue when whole arm movements with large feedback forces are employed [17]. Previous studies addressing wrist movements during fMRI involved 1DOF tasks and lacked control or repeatability of wrist movements [3], [4]. Recently, a multi-DOF wrist pointing study was conducted using motion tracking, but did not have the capability of force feedback [5]. To the best of our knowledge, the MR-SoftWrist is the first MR-compatible haptic robot that can measure and support 2DOF wrist movements with complete control and MRI-compatibility validation, including validation with an actual fMRI experiment.

The MR-SoftWrist is a promising tool for neuroscientists to investigate human sensorimotor control under haptic guidance. In the future, this device will be used in experiments with impaired subjects to examine the effects of different force fields or robot-aided therapeutic protocols on brain reorganization promoting motor learning and neurorecovery. With a better understanding of brain plasticity of patients with neurological disorders, personalized treatments might be conducted, possibly increasing the specificity of movement-based robotic therapy after neurological injury.

## REFERENCES

- [1] N. K. Logothetis, "What we can do and what we cannot do with fMRI," *Nature*, vol. 453, no. 7197, pp. 869–878, 2008.
- [2] S. Ogawa, R. Menon, S.-G. Kim, and K. Ugurbil, "On the characteristics of functional magnetic resonance imaging of the brain," *Annu. Rev. Biophys. Biomol. Struct.*, vol. 27, pp. 447–474, 1998.
- [3] S. Schaal, D. Sternad, R. Osu, and M. Kawato, "Rhythmic arm movement is not discrete," *Nature Neurosci.*, vol. 7, no. 10, pp. 1136–1143, 2004.
- [4] S. C. Cramer, R. R. Benson, D. M. Himes, V. C. Burra, J. S. Janowsky, M. E. Weinand, J. A. Brown, and H. L. Lutsep, "Use of functional MRI to guide decisions in a clinical stroke trial," *Stroke*, vol. 36, no. 5, pp. 50–52, 2005.
- [5] L. Shmuelof, J. Yang, B. Caffo, P. Mazzoni, and J. W. Krakauer, "The neural correlates of learned motor acuity," *J. Neurophys.*, vol. 112, no. 4, pp. 971–980, 2014.
- [6] C. D. Takahashi, L. Der-Yeghian, V. Le, R. R. Motiwala, and S. C. Cramer, "Robot-based hand motor therapy after stroke," *Brain*, vol. 131, no. 2, pp. 425–437, 2008.
- [7] F. Sergi, H. I. Krebs, B. Groissier, A. Rykman, E. Guglielmelli, B. T. Volpe, and J. D. Schaechter, "Predicting efficacy of robot-aided rehabilitation in chronic stroke patients using an MRI-compatible robotic device," in *IEEE Int. Conf. Eng. Med. Biol. Soc. (EMBC)*, 2011, pp. 7470–7473.
- [8] J. Sulzer, J. Duenas, P. Stampili, M.-C. Hepp-Reymond, S. Kollias, E. Seifritz, and R. Gassert, "Delineating the whole brain BOLD response to passive movement kinematics," in *IEEE Int. Conf. Rehab. Robot. (ICORR)*, 2013, pp. 1–5.
- [9] A. C. Lo, P. D. Guarino, L. G. Richards, J. K. Haselkorn, G. F. Wittenberg, D. G. Federman, R. J. Ringer, T. H. Wagner, H. I. Krebs, B. T. Volpe, C. T. Bever, D. M. Bravata, P. W. Duncan, B. H. Corn, A. D. Maffucci, S. E. Nadeau, S. S. Conroy, J. M. Powell, G. D. Huang, and P. Peduzzi, "Robot-assisted therapy for long-term upper-limb impairment after stroke," *New England J. Med.*, vol. 362, no. 19, pp. 1772–1783, May 2010.
- [10] R. Shadmehr and F. A. Mussa-Ivaldi, "Adaptive representation of dynamics during learning of a motor task," *J. Neurosci.*, vol. 14, no. 5, pp. 3208–3224, 1994.
- [11] R. Gassert, A. Yamamoto, D. Chapuis, L. Dovat, H. Bleuler, and E. Burdet, "Actuation methods for applications in MR environments," *Concepts Magn. Reson. B., Magn. Reson. Eng.*, vol. 29, no. 4, pp. 191–209, 2006.
- [12] R. M. Birn, R. W. Cox, and P. A. Bandettini, "Experimental designs and processing strategies for fMRI studies involving overt verbal responses," *NeuroImage*, vol. 23, no. 3, pp. 1046–1058, 2004.
- [13] N. Yu, C. Hollnagel, P. Wolf, W. Murr, A. Blickenstorfer, S. Kollias, and R. Riener, "Tracking and analysis of human head motion during guided fMRI motor tasks," in *IEEE Int. Conf. Rehab. Robot. (ICORR)*, 2009, pp. 588–593.
- [14] J. Diedrichsen, Y. Hashambhoy, T. Rane, and R. Shadmehr, "Neural correlates of reach errors," *J. Neurosci.*, vol. 25, no. 43, pp. 9919–9931, 2005.
- [15] N. Yu, C. Hollnagel, A. Blickenstorfer, S. S. Kollias, and R. Riener, "Comparison of MRI-compatible mechatronic systems with hydrodynamic and pneumatic actuation," *IEEE/ASME Trans. Mechatronics*, vol. 13, no. 3, pp. 268–277, 2008.
- [16] D. Campolo, D. Formica, E. Guglielmelli, and F. Keller, "Kinematic analysis of the human wrist during pointing tasks," *Exp. Brain Res.*, vol. 201, no. 3, pp. 561–573, 2010.
- [17] R. Gassert, L. Dovat, O. Lamercy, Y. Ruffieux, D. Chapuis, G. Ganesh, E. Burdet, and H. Bleuler, "A 2-DOF fMRI compatible haptic interface to investigate the neural control of arm movements," in *IEEE Int. Conf. Robot. Autom. (ICRA)*, 2006, pp. 3825–3831.
- [18] S. Menon, G. Brantner, C. Aholt, K. Kay, and O. Khatib, "Haptic fMRI: Combining functional neuroimaging with haptics for studying the brain's motor control representation," in *Int. Conf. IEEE Eng. Med. Biol. Soc. (EMBC)*, 2013, pp. 4137–4142.
- [19] M. A. Ergin, M. Kuhne, A. Thielscher, and A. Peer, "Design of a new MR-compatible haptic interface with six actuated degrees of freedom," in *IEEE RAS & EMBS Int. Conf. Biomed. Robot. Biomech. (BioRob)*, 2014, pp. 293–300.
- [20] A. Erwin, M. K. O'Malley, D. R. Renshaw, and F. Sergi, "Development, control, and MRI-compatibility of the MR-SoftWrist," in *IEEE Int. Conf. Rehab. Robot. (ICORR)*, 2015, pp. 187–192.
- [21] F. Sergi, A. Erwin, and M. K. O'Malley, "Interaction control capabilities of an MR-compatible compliant actuator for wrist sensorimotor protocols during fMRI," *IEEE/ASME Trans. Mechatronics*, vol. 20, no. 6, pp. 2678–2690, 2015.
- [22] J. F. Veneman, R. Kruidhof, E. E. Hekman, R. Ekkelenkamp, E. H. Van Asseldonk, and H. Van Der Kooij, "Design and evaluation of the LOPES exoskeleton robot for interactive gait rehabilitation," *IEEE Trans. Neural Syst. Rehab. Eng.*, vol. 15, no. 3, pp. 379–386, 2007.
- [23] A. Gupta, M. K. O'Malley, V. Patoglu, and C. Burgar, "Design, control and performance of RiceWrist: A force feedback wrist exoskeleton for rehabilitation and training," *Int. J. Robot. Res.*, vol. 27, no. 2, pp. 233–251, 2008.
- [24] K.-M. Lee and D. K. Shah, "Kinematic analysis of a three-degrees-of-freedom in-parallel actuated manipulator," *IEEE J. Robot. Autom.*, vol. 4, no. 3, pp. 354–360, 1988.
- [25] J. C. Perry, J. Rosen, and S. Burns, "Upper-limb powered exoskeleton design," *IEEE/ASME Trans. Mechatronics*, vol. 12, no. 4, pp. 408–417, 2007.
- [26] A. L. Pando, H. Lee, W. B. Drake, N. Hogan, and S. K. Charles, "Position-dependent characterization of passive wrist stiffness," *IEEE Trans. Biomed. Eng.*, vol. 61, no. 8, pp. 2235–2244, 2014.
- [27] H. Vallery, J. Veneman, E. Van Asseldonk, R. Ekkelenkamp, M. Buss, and H. Van Der Kooij, "Compliant actuation of rehabilitation robots," *IEEE Robot. & Autom. Mag.*, vol. 15, no. 3, pp. 60–69, 2008.
- [28] F. H. Ghorbel, O. Chételat, R. Gunawardana, and R. Longchamp, "Modeling and set point control of closed-chain mechanisms: Theory and experiment," *IEEE Trans. Contr. Syst. Technol.*, vol. 8, no. 5, pp. 801–815, 2000.
- [29] F. H. Ghorbel, R. Gunawardana, and J. B. Dabney, "Experimental validation of a reduced model based tracking control of parallel robots," in *IEEE Int. Conf. Contr. Appl. (CCA)*, 2001, pp. 375–382.
- [30] E. Burdet, R. Osu, D. W. Franklin, T. E. Milner, and M. Kawato, "The central nervous system stabilizes unstable dynamics by learning optimal impedance," *Nature*, vol. 414, no. 6862, pp. 446–449, 2001.
- [31] A. Melendez-Calderon, L. Masia, R. Gassert, G. Sandini, and E. Burdet, "Force field adaptation can be learned using vision in the absence of proprioceptive error," *IEEE Trans. Neural Syst. Rehab. Eng.*, vol. 19, no. 3, pp. 298–306, 2011.
- [32] F. Sergi, A. Erwin, M. K. O'Malley, C. L. Johnson, and D. Renshaw, "Quantitative testing of fMRI compatibility of mechatronic devices for sensorimotor protocols," *Submitted to IEEE Trans. Biomed. Eng.*, 2016.
- [33] A. U. Pehlivan, F. Sergi, A. Erwin, N. Yozbatiran, G. E. Francisco, and M. K. O'Malley, "Design and validation of the RiceWrist-S exoskeleton for robotic rehabilitation after incomplete spinal cord injury," *Robotica*, vol. 32, pp. 1415–1431, 2014.
- [34] H. I. Krebs, B. T. Volpe, D. Williams, J. Celestino, S. K. Charles, D. Lynch, and N. Hogan, "Robot-aided neurorehabilitation: A robot for wrist rehabilitation," *IEEE Trans. Neural Syst. Rehabil. Eng.*, vol. 15, no. 3, pp. 327–335, 2007.
- [35] T. L. Brooks, "Telerobotic response requirements," in *IEEE Int. Conf. Syst., Man, Cybern.*, 1990, pp. 113–120.
- [36] F. Sergi and M. K. O'Malley, "On the stability and accuracy of high stiffness rendering in non-backdrivable actuators through series elasticity," *Mechatronics*, vol. 26, pp. 64–75, 2015.
- [37] N. Nishitani, M. Schürmann, K. Amunts, and R. Hari, "Broca's region: from action to language," *Physiol.*, vol. 20, no. 1, pp. 60–69, 2005.
- [38] M. Heiser, M. Iacoboni, F. Maeda, J. Marcus, and J. C. Mazziotta, "The essential role of Broca's area in imitation," *Eur. J. Neurosci.*, vol. 17, no. 5, pp. 1123–1128, 2003.
- [39] R. Shadmehr and J. W. Krakauer, "A computational neuroanatomy for motor control," *Exp. Brain Res.*, vol. 185, no. 3, pp. 359–381, 2008.
- [40] A. Hribar and M. Munih, "Development and testing of fMRI-compatible haptic interface," *Robotica*, vol. 28, no. 2, pp. 259–265, 2010.